nature communications



Article

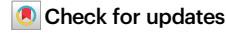
https://doi.org/10.1038/s41467-025-64673-8

Continuous time crystal coupled to a mechanical mode as a cavity-optomechanics-like platform

Received: 31 January 2025

Accepted: 22 September 2025

Published online: 16 October 2025



J. T. Mäkinen ^{1,2} □, P. J. Heikkinen ^{1,3}, S. Autti ^{1,4}, V. V. Zavjalov^{1,4} & V. B. Eltsov ¹

Time crystals are an enigmatic phase of matter in which a quantum mechanical system displays repetitive, observable motion – they spontaneously break the time translation symmetry. On the other hand optomechanical systems, where mechanical and optical degrees of freedom are coupled, are well established and enable a range of applications and measurements with unparalleled precision. Here, we connect a time crystal formed of magnetic quasiparticles, magnons, to a mechanical resonator, a gravity wave mode on a nearby liquid surface, and show that their joint dynamics evolves as a cavity optomechanical system. Our results pave way for exploiting the spontaneous coherence of time crystals in an optomechanical setting and remove the experimental barrier between time crystals and other phases of condensed matter.

Time crystals can be divided into two broad classes depending on whether they break the discrete or continuous time translation symmetry; the former is called a discrete time crystal, while the latter is known as a continuous time crystal (CTC). The concept of time crystals comes very close to a perpetual motion machine¹⁻³; spontaneous breaking of continuous time-translation symmetry requires a nonequilibrium system owing to the no-go theorem^{3,4}. For this reason, experimental realisations of time crystals are never in true equilibrium. The majority of existing CTC realisations utilise continuous pumping to bring the system out of equilibrium⁵⁻⁹, albeit pump-less realisations based on quasiparticles with finite lifetime^{10,11} are perhaps the closest analogue to the original time crystal idea¹. Overall, time crystals (both continuous and discrete) have been created in a range of physical systems⁵⁻¹⁷ and coupled to other time crystals^{18,19}, but always in isolation from their environment. Their inherent long-term coherence⁷ and versatility²⁰, in particular, is yet to be investigated with coupled external degrees of freedom.

In this work, we realise controlled interaction between a CTC^{5-11,11,17} and a well-defined external mechanical degree of freedom. We find that the coupled dynamics of the two periodic processes, the internal motion in the time crystal and the mechanical oscillations, form an optomechanical-like system^{21,22}. Optomechanics comes with rich and

well-understood phenomenology that enables analysing the coupling and its effects on the time crystal in detail. We utilise a time crystal formed of magnetic quasiparticles of superfluid ³He, magnons, interacting with a nearby liquid surface. We show that the time crystal frequency is modulated by the motion of the free surface, providing a key component of a cavity optomechanical system. Finally, we find that the coupling is nonlinear and tunable, enabling access to different regimes of optomechanics.

Results and discussion

Experimental realisation of the CTC

In our experiments magnons are trapped in the superfluid bulk by the combined effect of the order parameter distribution of the superfluid and the magnetic field profile, as illustrated in Fig. 1a. We pump non-equilibrium magnons into this system using a short (-1 ms) radio frequency (RF) pulse at a frequency close to but above the Larmor frequency $|\gamma|H\approx 833\,\mathrm{kHz}$, where γ is the gyromagnetic ratio of $^3\mathrm{He}$ and $H\approx 25\,\mathrm{mT}$ is the magnitude of the applied magnetic field. All further evolution proceeds without external pumping. As the pump has been turned off, the precessing individual magnons quickly dephase (in about 3 ms) due to the spatial profile of H. As partial equilibrium within the magnon subsystem is established, magnons condense to the

¹Low Temperature Laboratory, Department of Applied Physics, Aalto University, Espoo, Finland. ²QTF Centre of Excellence, Department of Applied Physics, Aalto University, Espoo, Finland. ³Department of Physics, Royal Holloway, University of London, Egham, Surrey, UK. ⁴Department of Physics, Lancaster University, Lancaster, UK. ⊠e-mail: jere.makinen@aalto.fi

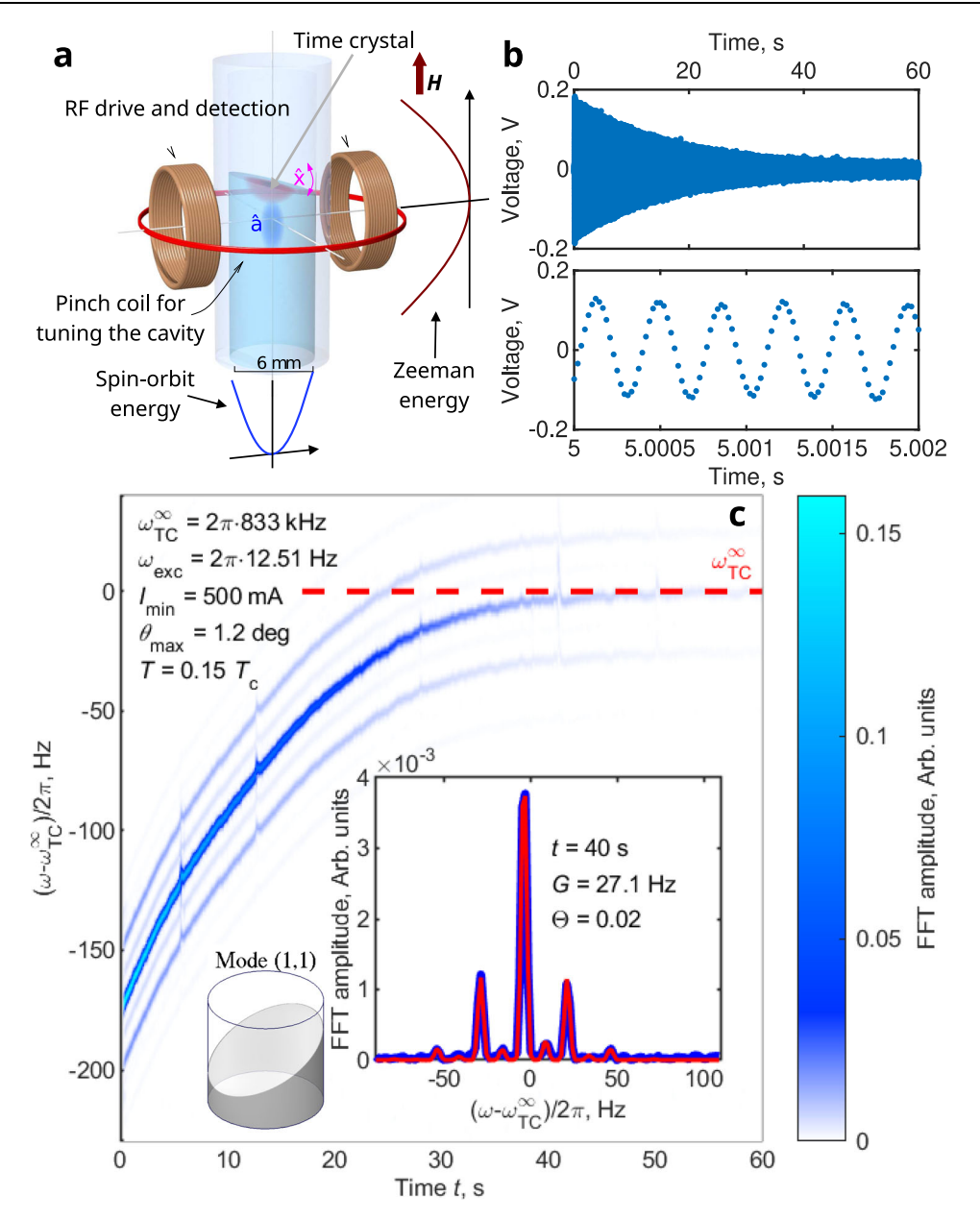


Fig. 1 | **Time crystal with optomechanics-like coupling. a** The CTC is formed of magnons (represented by operator \hat{a}) that are spatially trapped by the combined effect of the spin-orbit energy related to order parameter distribution (radial direction) and Zeeman energy controlled by the magnetic field profile (axial direction). The magnetic field profile **H** is used to move the CTC against the free surface (red blob inside the container) or within the bulk liquid (blue blob inside the container). The CTC couples to externally driven surface wave mode (represented by the position operator \hat{x}). **b** The precession of magnetisation within the time crystal is observed as an induced, decaying sinusoidal voltage in the pick-up coils, recorded with downconversion in frequency. **c** A sliding windowed fast Fourier

transform (FFT) of the signal with on-resonance mechanical forcing reveals that the CTC signal is accompanied by sidebands. The sidebands result from the frequency modulation of the time crystal signal, caused by the motion of the free surface. The red dash line indicates the mean frequency of the time crystal in the limit of vanishing magnon number $\omega_{\text{TC}}^{\infty} = \langle \omega_{\text{TC}}(t \to \infty) \rangle$. The measurements of the optomechanical coupling are carried out in this limit. The large inset shows a snapshot of the signal (blue points), including the fitted spectrum shape (red line) and parameter values in the region where the time crystal's frequency has ceased changing. The fit details are explained in Methods. The fundamental surface wave mode driven in this Article is depicted in the small inset.

ground level in the trap with a typical time scale of $-0.1\,\mathrm{s}$, forming a Bose-Einstein condensate (BEC). The BEC of magnons is characterised by coherent precession of spins of all condensed magnons with a common frequency ω_{TC} , spontaneously breaking the continuous time translation symmetry and thus forming the CTC. It is worth noting that $\hbar\omega_{\mathrm{TC}}$ is simultaneously the magnon chemical potential as determined by the ground state energy of the trapping potential^{23,24}. In experiments, the coherent precession is manifested as an oscillating voltage induced in the RF coils by electromagnetic induction, Fig. 1b. While

magnons slowly decay, the CTC preserves its coherent state for up to a few minutes, or about 10^8 cycles.

The optomechanical-like system

In the paradigmatic optomechanical system, the optical cavity is formed of two mirrors, one of them fixed and the other attached to a spring, allowing the mirror to move. In this setting, the cavity resonance frequency changes linearly with the position of the mirror, and radiation pressure couples the optical and mechanical degrees of

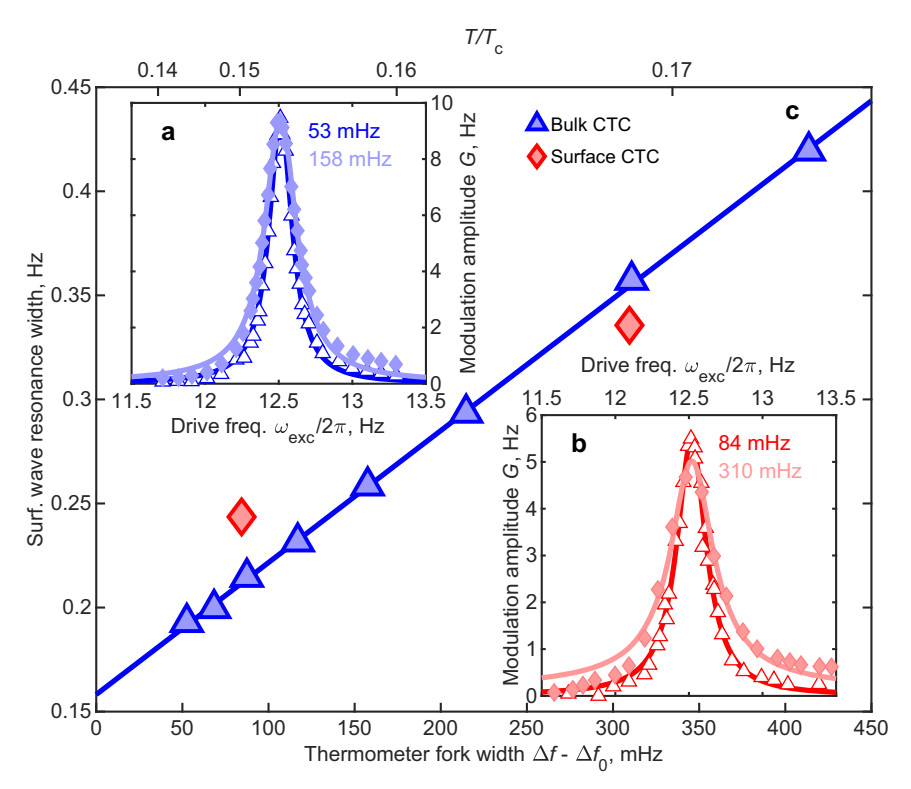


Fig. 2 | **The mechanical mode. a** The frequency modulation amplitude $G = g\theta_{\text{max}}^2$ of the bulk time crystal measured as a function of the mechanical forcing frequency ω_{exc} . The solid lines are fits to a driven and damped harmonic oscillator response, from which the resonance frequency and width of the mechanical surface wave mode are determined. The thermometer fork width Δf relative to the intrinsic width Δf_0 of the device for the two data sets is given in the legend. In the shown temperature interval the on-resonance amplitude G remains approximately constant despite exponentially increasing resonance width, suggesting that coupling increases with the same exponent as a function of temperature. Here, unlike other measurements in this Article, the magnon number was kept constant by applying continuous pumping to an excited state in the confining trap¹⁰, as extremely long

lifetime of bulk time crystal makes pulsed spectral measurements impractical. **b** Data measured for the surface time crystal are extracted from the end of the decay after an RF excitation pulse, where the time crystal's frequency has stopped changing. **c** The extracted width of the surface wave resonance (points) scales linearly with the the thermometer fork resonance width (solid line). This confirms that the damping of the mechanical mode that is coupled to the time crystal mainly originates from scattering of thermal excitations in the superfluid. The *y*-axis intercept corresponds to the mechanical mode dissipation in the absence of superfluid thermal excitations, which may be caused by friction on the container walls or by the edge states bound to the free surface of the topological superfluid.

freedom. Here, the time crystal is located in the vicinity of a free surface of the superfluid, where gravity waves of the surface make a mechanical oscillator. For small gravity wave amplitudes, the surface is tilted uniformly and oscillates back and forth. The surface motion modifies the superfluid order parameter distribution and, therefore, the time crystal frequency. We can write the time crystal frequency as (See Methods).

$$\omega_{\text{TC}}(t) = \omega_0 + 2\pi g \times (\theta(t) - \theta_0)^2, \qquad (1)$$

where ω_0 is the time crystal's frequency when the free surface is orthogonal to the container axis, g is an optomechanical coupling constant, t is time, and $\theta(t)$ – θ_0 is the angle between the container axis and the surface normal. We have allowed for a small asymmetry θ_0 describing the tilt of the container axis relative to gravity in the absence of surface motion. For small-amplitude surface waves close to the container axis $\theta(t,\omega_{\rm exc})$ = $\theta_{\rm max}(\omega_{\rm exc})\sin(\omega_{\rm exc}t)$, where $\omega_{\rm exc}$ is the drive frequency and $\theta_{\rm max}(\omega_{\rm exc})$ characterises the frequency-dependent surface oscillation amplitude. We note that Eq. (1) allows tuning between quadratic ($\theta_0 \ll \theta_{\rm max}$) and linear ($\theta_0 \gg \theta_{\rm max}$) coupling by using θ_0 as a control parameter, providing access to dispersive optomechanics²⁵.

We control the position of the time crystal magnetically using a pinch coil. The time crystal can be positioned so that it is in the direct vicinity of the free surface, or in the bulk of the superfluid a few mm

below the surface 18,19 . In these two cases, the physical mechanism behind the coupling g of the time crystal to the moving free surface is qualitatively different as discussed later in the Article. In all other respects the location makes no difference to the interpretation of the data.

Here, we drive the mechanical mode by moving the sample container nearly horizontally (See Methods) with constant amplitude throughout formation and decay of the CTC. We use windowed Fourier transform of the pick-up signal for inferring the time crystal dynamics, Fig. 1c. The time crystal signal exhibits sidebands with the intensity which depends on the strength of the drive of the mechanical mode. These sidebands result from the optomechanical-like frequency modulation of ω_{TC} , caused by the motion of the superfluid free surface. A reconstruction of the experimental signal (inset in Fig. 1c) allows extracting the products $G \equiv g\theta_{\text{max}}^2$ and $\Theta \equiv \theta_0\theta_{\text{max}}^{-1}$ as explained in Methods. Note that the CTC frequency is also increasing slowly across half a minute by about 150 Hz before becoming stable. This is because local magnon density modifies the order parameter part of the trap²⁶, and the magnon number slowly decreases during the experiment due to dissipation²⁷. We note that because of the very long life time of the time crystal and the changing frequency, the time crystal line width is determined by the length of the Fourier time window, not the time crystal quality factor. As such, the sideband width is not a measure of the dissipation of the mechanical mode, unlike in paradigmatic optomechanical systems²¹.

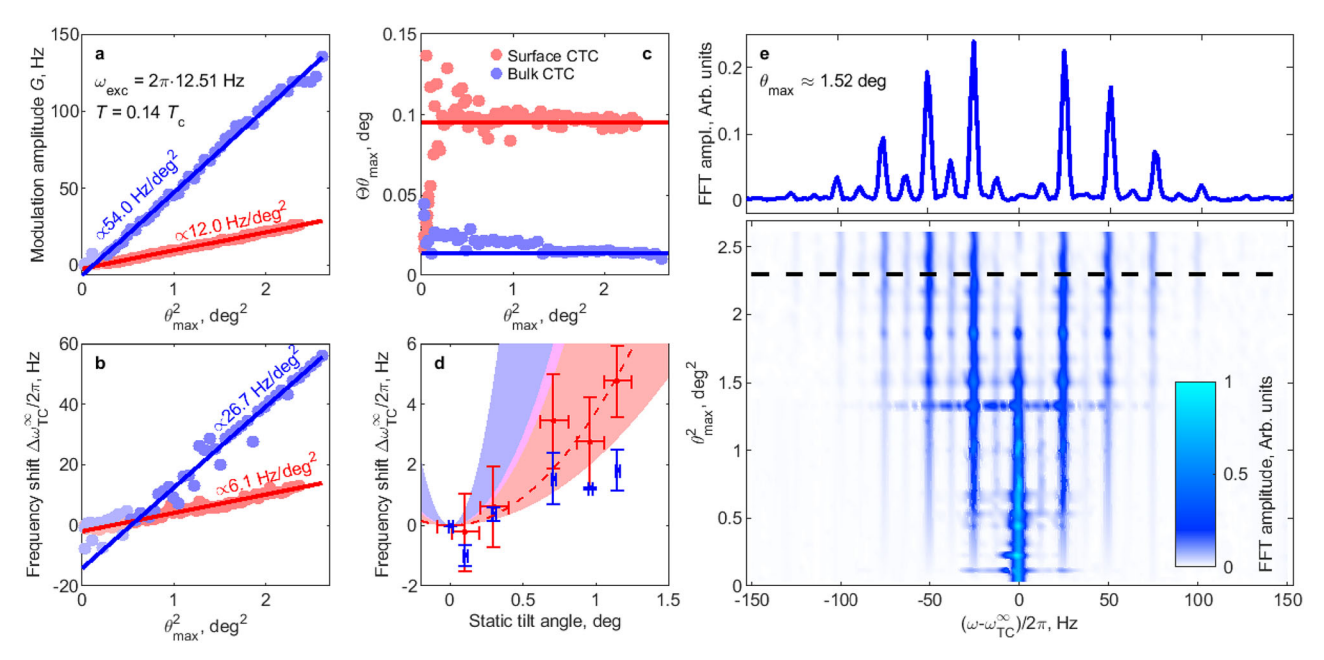


Fig. 3 | **The optomechanical coupling mechanisms. a** With on-resonance mechanical forcing, the fitted time crystal frequency modulation amplitude G (points) is found to depend linearly on θ_{\max}^2 (fitted lines). **b** The mean frequency shift $\Delta\omega_{TC}^{\infty} = (\omega_{TC}^{\infty}(\theta_{\max}) - \omega_{TC}^{\infty}(\theta_{\max} = 0))$ is half of the frequency modulation amplitude, in agreement with Eq. (1). **c** The product of the fitted asymmetry θ and θ_{\max} (points) is found to be independent of the mechanical motion amplitude, as expected if θ_0 originates from misalignment of the surface normal and container axis. Solid horizontal lines are a guide to the eye. **d** As a function of the static tilt angle, the surface time crystal frequency shift (points) is consistent with the coupling constant g_{surf} between 2.2 and 12.0 Hz deg⁻² determined from dynamic measurements (red and magenta shaded regions). The static shift for the bulk time crystal (points) is smaller than expected from the dynamic measurements (blue and

magenta shaded regions) with $g_{\rm bulk}$ in the range from 9.8 to 54.0 Hz deg⁻², showing that the optomechanical coupling is enhanced significantly in the dynamic case. The red dash line is a fit to points with $g_{\rm surf} = 3.74$ Hz deg⁻². The horizontal error bars correspond to the value of the static tilt from ${\bf c}$ and the vertical error bars correspond to one standard deviation for measurements performed at different minimum coil currents ($N_{\rm surface} = 8$, $N_{\rm bulk} = 3$). ${\bf e}$ Bottom: Larger mechanical forcing amplitude results in larger frequency modulation, reflected in the number and amplitude of the side bands seen in the Fourier spectrogram of the time crystal signal. Top: For the largest free surface motion amplitudes the time crystal frequency modulation becomes large enough to completely diminish the central frequency band corresponding to $\omega_{\rm TC}^{\infty}$. The black dashed line in the bottom panel shows where this individual frequency spectrum lies in the plot below.

Characterisation of the mechanical mode

We use the time crystal to characterise the mechanical mode by sweeping the frequency of the mechanical forcing across the surface gravity wave resonance and recording the modulation amplitude of the time crystal frequency. The response is centred at \approx 12.5 Hz (Fig. 2a, b), which agrees well with the theoretical expectation for surface waves in this geometry, within 0.1 Hz (See Methods).

The width of the surface wave resonance (its dissipation) is found to increase linearly with the quasiparticle density in the superfluid (Fig. 2c). This observation connects the time crystal to the motion of the free surface beyond doubt, since the mechanical dissipation in the superfluid is caused by scattering of thermal excitations from the moving surface²⁸. The fermionic quasiparticle density can be measured separately by a tuning fork resonator, whose resonance width at low temperatures is linearly proportional to the quasiparticle density²⁹, which in turn depends exponentially on temperature. Based on the matching resonance frequency and the observed linear dependence between the surface wave resonance width and that of the tuning fork's, we conclude that the observed resonance is connected with motion of the superfluid surface.

The dissipation of the free surface oscillation releases heat into the superfluid, the amount of which depends on the drive power. We can measure the resulting temperature gradient in the superfluid by using the time crystal as a thermometer 30 and comparing this with the reading of a separate tuning fork thermometer at the bottom of the sample container cylinder. The typical temperature increase at the free surface is a few μ K, which corresponds to a few pW of heating power 31 . The extracted heating is then converted into the maximum surface tilt

angle $\theta_{\rm max}$, which provides an independent measurement of the amplitude of the surface oscillations (See Methods).

Determining the nature of optomechanical-like coupling

With direct access to the mechanical mode amplitude, we now compare the coupling in Eq. (1) with observations. Figure 3a shows that the measured time crystal frequency modulation amplitude G is proportional to the square of the measured mechanical mode amplitude θ_{max}^2 . For sinusoidal mechanical oscillations coupled quadratically to the time crystal as in Eq. (1), the mean frequency of the time crystal is expected to be shifted by half of the modulation amplitude. This is confirmed by Fig. 3b. Increasing the amplitude of the mechanical forcing leads to increased amplitude of the frequency modulation of ω_{TC} , seen as higher-order side bands appearing and eventually the central band disappearing as shown in Fig. 3e. In line with our interpretation of θ_0 , panel c in Figure 3 shows that the product of the fitted asymmetry Θ and θ_{max} , i.e. $\theta_0 = \Theta \times \theta_{\text{max}}$, for both the bulk and surface time crystals, is independent of the mechanical mode amplitude. Together, these observations confirm that the coupling follows Eq. (1).

Finally, we can identify different contributions to the optomechanical-like coupling comparing the bulk and surface time crystal responses to applied static tilt of the free surface. Within experimental uncertainties, the surface time crystal frequency shift, and thus coupling g_{surf} , is the same whether the tilt is static or dynamic (Fig. 3d). This implies that the surface time crystal frequency follows quasi-static changes in the confining trap as determined by the motion of the surface. The bulk time crystal coupling g_{bulk} is smaller than the surface coupling if only static tilt is applied. This is reasonable as the

effect of the tilted surface, via the order parameter part of the trapping potential, is felt less further away from the surface.

With dynamic tilt, however, the bulk coupling is enhanced by more than an order of magnitude. Additionally, this enhancement increases with temperature, as can be seen in Fig. 2a, where larger mechanical line width at higher temperature does not reduce the measured signal in resonance. The additional coupling is caused by the superfluid flow linked to the surface displacement. This flow modifies the order parameter spatial distribution, and the magnitude of the effect depends exponentially on temperature^{32,33}. The surface time crystal does not react to the flow, because close to the surface, the boundary condition rigidifies the order parameter trap^{18,19} and thus the superflow is not able to change the trap shape. Postulating coincidence of dynamic and static coupling for the surface time crystal, we can estimate that at the lowest measured temperatures, about 70% of the heat dissipated by the moving free surface is carried away by surfacebound Andreev states³⁴. Theoretical details and a phenomenological derivation supporting the above findings can be found in Methods. We also note that the measured asymmetry of the coupling in Fig. 3c is smaller for the bulk time crystal than for the surface one. This has natural explanation as the residual static tilt of the container axis with respect to gravity becomes less important for the bulk time crystal, where the coupling is mostly dynamic, due to superflow.

Discussion and outlook

Based on the observations reported in this Article, we conclude that continuous time crystals can be coupled to a macroscopic mechanical oscillator and that the resulting coupled dynamics are described by an optomechanical-like Hamiltonian, thus combining the inherent coherence of time crystals with the sensitivity of optomechanical systems. We suggest to call such methodology time crystal optomechanics. The underlying idea, tuning the CTC period by coupling to an external degree of freedom, is very general, and we expect that time crystal optomechanics can be realised in other physical systems⁹. This will open new avenues for research on time crystals as optomechanical systems have shown the capacity to push the boundaries of both fundamental and applied physics³⁵, for example, via measuring weak forces³⁶⁻³⁸, cooling mechanical degrees of freedom down to their ground state³⁹, and even entangling them⁴⁰. Replacing the cavity of an optomechanical system with a CTC may allow similar applications in parameter ranges (e.g. in terms of temperatures, frequencies and/or coherence times) inaccessible in traditional optomechanical systems. Although our scheme is not directly applicable to discrete time crystals (DTCs), it is also an interesting question whether new avenues can be opened by coupling a DTC to a mechanical mode. 16,41

In our present system, the optomechanical coupling is found to be predominantly quadratic⁴², but is expected to be tuneable all the way to linear by adjusting θ_0 . We also note that the frequency modulation scheme in our experiments is similar to frequency comb generation using a modulated continuous wave laser⁴³, paving way for utilising time crystals for precision spectroscopy⁴⁴. For suitably chosen large mechanical drive amplitudes the system becomes transparent at the time crystal's central frequency, Fig. 3e. Control over the transparency of a truly macroscopic and long-living quantum state may prove useful for example for quantum state storage⁴⁵, as the system additionally has continuously tunable central frequency (via magnetic field) and band separation (via cylinder radius or coupling to another type of mechanical resonator). We also note that the underlying physical system is a topological superfluid, providing wide possibilities from dark matter research^{46,47} to detection of topological defects^{48,49} using the optomechanical time crystal system as an instrument.

Applications of optomechanics to a large extent rely on the sufficiently strong coupling between optical and mechanical modes or, in other words, sufficiently strong backreaction through the radiation pressure. This allows manipulation of the mechanical mode, including its quantum state, via the optical cavity, Following this idea, we can estimate the performance of our system in a similar manner: The surface tilt θ_1 , corresponding to a single ripplon, can be estimated from $E(\theta_1) \sim \hbar \omega_{SW}$ (see Eqs. (M3) and (M6)) as $\theta_1 \sim 3 \cdot 10^{-11}$ degrees. This tilt results in the CTC frequency shift $g_1 = 2g\theta_0\theta_1 \sim 10^{-10}$ Hz, which is much smaller that the "cavity" (CTC) decay rate κ ~10⁻² s. For many practical applications, the light-enhanced (here, magnon-enhanced) coupling $g_1\sqrt{N}$, where N is the number of the quanta in the cavity, is the relevant parameter²¹. With a typical magnon number $N \sim 10^{12}$ in the CTC in our experiment, even this scaled coupling is below κ . The backreaction force from the magnon CTC to the free surface is $F_{\text{magn}} = \hbar \partial \omega_{\text{TC}} / (R \partial \theta)$ N ~10⁻¹⁸ N is much smaller than the mechanical damping force $F_{\rm damp} \sim E(\theta_{\rm max})/(QR\theta_{\rm max}) \sim 10^{-8}\,{\rm N}$ and thus is not directly observable. Nevertheless, even with these limitations, we have characterised surface waves in the coldest ever glass of liquid.

Importantly, the limitations of our present setup, not optimised for optomechanics, are not fundamental. Time crystal optomechanics could be realised in the quantum regime and can also achieve strong coupling by using nanoelectromechanical resonators as the mechanical degree of freedom⁵⁰. Such devices have significantly lower mass than the surface waves in this work, and can be designed to have orders of magnitude larger resonance frequencies and quality factors, both of which are essential for reaching the quantum regime. Potentially, such a setup allows for mechanical resonance frequencies matching or even exceeding the optical mode frequency, yielding access to the mechanical dynamical Casimir effect^{51,52} and yet unexplored regimes of optomechanics. Moreover, an attached micromagnet could be utilised to drastically enhance coupling with the magnonic time crystal. We emphasise that similar research avenues may be accessible also at room temperature by utilising suspended yttrium-iron-garnet (YIG) film resonators⁵³, which can host magnon time crystals at room temperature^{54,55}. Thus, our work paves way for utilising time crystals as tools for research, and as an integral part of hybrid systems for quantum technology.

Methods

Experimental setup

The sample container we use is a cylindrical quartz-glass tube (15 cm long, 2R = 5.85 mm diameter, Fig. 1). The 3 He placed in the cylinder is cooled down by a nuclear demagnetisation refrigerator into the superfluid B phase. The lower end of the sample container connects to a volume of sintered silver powder surfaces, thermally linked to the nuclear refrigerant. This allows cooling the 3 He in the cylinder down to $130 \, \mu K$.

Temperature of the superfluid is measured using a quartz tuning for $k^{29,56}$, immersed in the superfluid. In the low-temperature regime investigated in this manuscript, the fork's resonance width depends linearly on the thermal excitation density, which in turn depends on temperature as $\propto \exp(-\Delta/k_BT)$, where Δ is the superfluid gap and k_B is the Boltzmann constant. Additionally, we can utilise the relaxation rate of the bulk time crystal as a thermometer k_B 0 its relaxation rate likewise depends exponentially on temperature, k_B 1 k_B 2.

The pressure of the superfluid sample is equal to saturated vapour pressure, which is vanishingly small at these low temperatures. The superfluid transition temperature at this pressure is $T_{\rm c}\approx 0.93$ mK. The transverse nuclear magnetic resonance (NMR) pick-up coil, placed around the sample container, is part of a tank circuit resonator with the quality factor of about 150. The setup includes also a pinch coil to create a minimum along the vertical axis of the otherwise homogeneous axial magnetic field. The resonance frequency of the tank circuit is 833 kHz in all measurements presented in this paper, corresponding to an external magnetic field of 25 mT. We use a cold preamplifier and room temperature amplifiers to amplify the voltage induced in the NMR coils.

The free surface is positioned 3 mm above the location of the magnetic field minimum. We adjust the liquid level by removing ³He starting from the originally fully filled sample container while measuring the pressure of ³He gas in a calibrated volume.

The time crystals are created by a short (-1 ms) excitation pulse via the NMR coils. The pulse is resonant with an excited state in the trap that confines the magnons (details of the trap are described below). In about 0.1 s, well after the end of the pump pulse, the magnons spontaneously form a time crystal on the ground state of the trap in a Bose-Einstein condensate phase transition. The time crystal frequency and magnon number can be inferred from the AC voltage induced in the NMR coils, originating from the coherent precession of magnetisation in the time crystal at $\omega_{\rm TC}$. Details of the time crystal wave functions and signal readout are explained in ref. 11 and the Methods sections of Refs. 18,19.

Signal analysis

The precession of magnetisation in the time crystal produces a voltage signal in the pick-up coils. This signal is fed to a lock-in amplifier, which is typically locked 2–3 kHz above the time crystal's precession frequency and is thus used for the frequency downconversion. The lock-in output is sampled at 48 kHz frequency. An example of such frequency-shifted record is shown in Fig. 1b. We transform the wave record to frequency space by a windowed fast Fourier transformation (FFT) with a 3×10^4 point window size and a 10% shift between windows.

We then trace the frequency of the central band in the FFT signal in time. In most cases this is the maximum of the FFT signal, but care should be taken at large mechanical drive amplitudes, where the sideband amplitude may exceed the central band amplitude. This trace is then used by the fitting algorithm.

The amplitude of the FFT spectrum is fit separately in each window to the FFT of the model signal $U(t) = A \sin \int_0^t \omega_{\text{TC}}(t') dt'$ with ω_{TC} from Eq. (1) and $\theta(t) = \theta_{\text{max}} \sin \omega_{\text{exc}} t$. The surface modulation frequency ω_{exc} is determined from the FFT of the geophone record (see the next section), measured simultaneously with the time crystal signal. There are four fitting parameters: the overall amplitude A, combinations $G = g\theta_{\text{max}}^2$ and $\Theta = \theta_0\theta_{\text{max}}^{-1}$ describing coupling to the surface mode and the average frequency $\langle \omega_{\text{TC}} \rangle$. Note that it is important for the proper fit to allow ω_0 in Eq. (1) to depend on time as magnons are decaying from the trap, since the widths of the spectral bands are affected by this time dependence, especially near the beginning of the signal. From a single fitting parameter $\langle \omega_{\text{TC}} \rangle$ for a window, we model $\omega_0(t)$ using time dependence of the traced frequency described above.

Mechanical forcing and calibration

A simplified schematic of the sample positioning and the mechanical support is shown in Supplementary Fig. 1 (See Supplemental Information). The cryostat is levitated on top of four active air spring dampers with attached distance sensors. These dampers are normally used to isolate the cryostat from mechanical vibrations in the surrounding support structures. The sensors feed their output to a proportional-integral-derivative (PID) controller. To induce mechanical forcing, we modulate the set point of one of the air springs as $A_{\text{nom}} \sin(\omega_{\text{exc}}t)$ resulting in small deviations of the cryostat's tilt angle with the drive frequency ω_{exc} . The air springs are located at 90 cm radius and approximately 1.65 metres above the liquid surface in the sample cell. The support frame itself is rigid, resulting in nearly horizontal oscillations of the sample. Similar mechanical forcing has been applied previously for surface wave studies in superfluid ³He and ⁴He²⁸.

We calibrate the tilt angle by attaching a laser pointer to the cryostat and applying a static tilt by changing the setpoint of the airspring we use for modulation. We then monitor the position of the laser pointer at fixed distance and calculate the corresponding tilt

angle. This way, we are able to apply tilt angles $\lesssim 1.2^{\circ}$. In dynamic measurements, the applied setpoint shifts are kept well below this value. For recording amplitude of the dynamic drive, the cryostat is equipped with the geophone. It is installed at room temperature on the level of the air spring dampers, and thus conversion of the geophone signal to the surface oscillation amplitude requires calibration described below.

We connect the nominal mechanical forcing amplitude $A_{\rm nom}$ to the motion of the cryostat using a voltage $V_{\rm gp}$ produced by the geophone. The result is shown in Supplementary Fig. 2 (See Supplemental Information) from the same data set as in Fig. 3 of the main text. We find that the mechanical motion amplitude is well described by a function of the form

$$V_{\rm on} = C \cdot A_{\rm nom}^{\nu} + B \,, \tag{M1}$$

which contains three fitting parameters: a scale factor C, free exponent ν , and constant B to allow for non-zero base level in the measured voltage.

Converting the mechanical forcing as measured by the geophone to excitation of the free surface motion can be done in three steps. If we drive the surface mode on resonance, the applied drive power is equal to dissipated power. The dissipation is observed as a heat flow into the superfluid, originating from the free surface motion. The resulting temperature gradient can be measured directly by comparing the temperature measured by the thermometer fork at the bottom of the container and using the time crystal as a thermometer at the top of the container³⁰, see Supplementary Fig. 3a (See Supplemental Information).

The temperature gradient can be converted to power using the known thermal conductivity of superfluid $^3\text{He-B}$ in a cylindrical container 31 . The thermal resistance of $^3\text{He-B}$ at similar experimental conditions (pressure, temperature, magnetic field) was measured to be $R_T' \approx 0.15\,\mu\text{K pW}^{-1}$ for a 5-cm-long cylindrical container with 8 mm diameter. Our cylindrical container has a \approx 6 mm diameter and the magnon condensate is located some \approx 14 cm above the bottom volume containing the thermometer fork. Scaling the thermal resistance with the lengths and inverse square radii, we get an estimate $R_T \approx 0.75\,\mu\text{K pW}^{-1}$ between the magnon time crystal and the heat exchanger volume in our experimental geometry.

The power can be converted into a range of motion as follows. The fraction of energy lost per cycle in a damped harmonic oscillator is

$$\frac{\Delta E}{E(\theta_{\text{max}})} = 1 - e^{-2\pi/Q} \tag{M2}$$

where Q is the quality factor of the oscillator. The quality factor estimated as the temperature dependent part of the dependence shown in Fig. 2 gives $Q \approx 375$, while the total quality factor, including the zero-temperature offset for the surface wave resonance width, is $Q \approx 65$. The gravity potential energy stored in the free surface motion at the maximum amplitude of the oscillation cycle is

$$E(\theta_{\text{max}}) = (\pi/8)\rho_{\text{He}}g_g R^4 \theta_{\text{max}}^2, \qquad (M3)$$

where $\rho_{\rm He}$ = 81.9 kg m⁻³ is the density of the superfluid⁵⁸ and $g_{\rm g}$ = 9.81 m s⁻² is the free-fall acceleration. Thus, the dissipation power becomes

$$P = \frac{\omega}{16} \left(1 - e^{-2\pi/Q} \right) \rho_{\text{He}} g_{\text{g}} R^4 \theta_{\text{max}}^2 \tag{M4}$$

which yields $P/\theta_{\rm max}^2 \approx 8.1~{\rm pW~deg^{-2}}$ for the total quality factor $Q \approx 65$. We can now express the measured temperature difference $\Delta \tilde{T}(A_{\rm exc}) = \Delta T_{\rm TC}(A_{\rm exc}) - \Delta T_{\rm fork}$, where $A_{\rm exc} = V_{\rm gp}(A_{\rm nom})/V_{\rm gp}(A_{\rm nom} = 0.098)$

is the normalised amplitude, as

$$\frac{\Delta \tilde{T}}{\theta_{\text{max}}^2} = \frac{R_{\text{T}}P}{\theta_{\text{max}}^2} \approx 6.1 \,\mu\text{K deg}^{-2} \,. \tag{M5}$$

Thus, drive amplitude is determined as $\theta_{\max}^2(\deg)^2 \approx \Delta \tilde{T}/6.1 \mu \text{K}$. To obtain direct relation between θ_{\max} and A_{exc} (and thus V_{gp}), we perform a single parameter fit shown in Supplementary Fig. 3b (See Supplemental Information), resulting in $\theta_{\max}^2(\deg)^2 \approx 2.62 A_{\text{exc}}$. In analysis and plotting of the data in the main text as a function of the drive amplitude θ_{\max} , we convert applied excitation A_{nom} to V_{gp} and then to θ_{\max} using calibration expressions above.

In Figure 3d the upper edge of the shaded areas correspond to the calibration obtained as explained above, using the full $Q \approx 65$. This calibration is used for θ_{max} scale in other panels of Fig. 3. In general, we may expect some of the dissipated heat to be carried away by a layer of surface bound states on the walls of the container and the free surface^{34,59}. The temperature-independent part of dissipation is generated at the surfaces. If all of this heat is carried away along the surface, never entering the bulk, then $Q \approx 375$ will be appropriate to calibrate the tilt angles instead. The lower edge of the shaded regions in Fig. 3d corresponds to this limit. It is plausible that only a part of the generated heat escapes the bulk, and these two extreme limits we take as uncertainty of the calibration, which determines uncertainty range of the determined optomechanical coupling g.

If we postulate that for the surface time crystal static and dynamic coupling coincide, we can fit the dynamic coupling to the static measurements to pick up a particular heat release fraction from the uncertainty band. The fit shown by the dashed line in Fig. 3d gives $g_{\rm surf} \approx 3.74~{\rm Hz~deg^{-2}}$. This value corresponds to 84% of the temperature-independent part of the dissipated heat being carried away by the surface bound states. From the total dissipation at the lowest experimental temperature this makes 69%.

Gravity wave resonances

For inviscid, incompressible, and irrotational flow, the dispersion of gravity waves in a cylindrical container much deeper than its diameter is given $by^{60}\,$

$$\omega_{\text{SW}}^2 = g_{\text{g}} k_i \left(1 + \frac{\sigma k_i^2}{g \rho_{\text{He}}} \right), \tag{M6}$$

where k_i is the wave number, and $\sigma = 155 \,\mu\text{N/m}$ is the surface tension of $^3\text{He}^{61}$.

The velocity field ${\bf u}$ related to a scalar potential ${\boldsymbol \phi}$ can be calculated as

$$\mathbf{u} = -\nabla \boldsymbol{\phi} \,. \tag{M7}$$

For an infinitely deep cylindrical container, the potential associated with the planar fundamental mode is⁶²

$$\phi = AJ_1(k_1r)e^{k_1z}\sin(\omega t)\sin(\varphi), \qquad (M8)$$

where $A = \omega_{\rm m}\theta_{\rm max}k_1^{-2}$ is the wave amplitude, J_i is the Bessel function of the first kind or order i, k_1 is the wave number of the fundamental mode, z is the vertical coordinate (z = 0 at fluid surface, negative values towards the fluid), and φ is the azimuthal angle.

The resulting velocity field is then

$$\mathbf{u} = -\frac{A}{2}k_1(J_0(k_1r) - J_2(k_1r))e^{k_1z}\sin(\omega t)\sin(\varphi)\hat{\mathbf{r}}$$

$$-\frac{A}{r}J_1(k_1r)e^{k_1z}\sin(\omega t)\cos(\varphi)\hat{\boldsymbol{\varphi}}$$

$$-AkJ_1(k_1r)e^{k_1z}\sin(\omega t)\sin(\varphi)\hat{\mathbf{z}},$$
(M9)

which additionally sets the magnitude of k_1 by requiring the radial flow to be zero at the container wall. In other words, the wave number k_1 is the first solution to equation

$$J_0(k_1R) - J_2(k_1R) = 0$$
, (M10)

setting $k_1 \approx 1.8412/R$.

Taking into account the meniscus effect, the gravity wave dispersion relation is modified $to^{\rm 63}$

$$\omega_{\text{SWm}}^2 = \omega_{\text{SW}}^2 \left(1 - \frac{2\sigma k_i}{g_g \rho_{\text{He}} R} \right). \tag{M11}$$

For the lowest mode with k_1 , we get $\omega_{\text{SWm}}/2\pi \approx 12.4$ Hz, in good agreement with experimental observations.

Surface wave oscillations near the container axis

The surface height profile of the first mode takes the form⁶⁴

$$h(r, \phi, t) = AJ_1(k_1 r) \sin(\omega t) \sin \varphi. \tag{M12}$$

To derive the maximum tilt angle during the time evolution of the surface wave, we set $\sin \varphi = 1$. We can estimate the tilt angle θ from the radial derivative of Eq. (M12):

$$\tan \theta = \frac{\partial h}{\partial r} = \frac{Ak_1}{2} \left[\left(J_0(k_1 r) - J_2(k_1 r) \right) \sin(\omega t) \right]. \tag{M13}$$

Solving for θ and taking the limit $r \to 0$ (the time crystal is located close to r = 0), to leading order we get

$$\theta_{r\to 0} \approx \arctan\left[\frac{Ak_1}{2}\sin(\omega t)\right] \approx \frac{Ak_1}{2}\sin(\omega t),$$
 (M14)

where the last approximation results from $Ak_{\rm l}/2 \ll 1$. Therefore, we arrive to

$$\theta(t) \approx \theta_{\text{max}} \sin(\omega t)$$
, (M15)

where we have set $\theta_{\rm max} \equiv Ak_1/2$. This is the time dependence used in the main text.

Magnon trapping potential

The axial trapping potential for (optical) magnons in the superfluid is set by the magnetic field profile as

$$U_{\parallel}(z)/\hbar = \omega_{\rm L}(z) = |\gamma|H(z), \tag{M16}$$

where ω_L is the local Larmor frequency and γ is the gyromagnetic ratio of ${}^3\text{He}$. The magnetic field profile is created with a solenoid creating a field with inhomogeneity on the level of 10^{-4} , and by a pinch coil which produces a local minimum in the magnetic field along the vertical axis, shown in Fig. 1.

The radial trapping potential is set by the textural configuration via the spin-orbit interaction

$$U_{\perp}(r)/\hbar = \frac{4\Omega_{\rm L}^2}{5\omega_{\rm L}}\sin^2\frac{\beta_{\rm L}(r)}{2}\,,\tag{M17}$$

where Ω_L is the B-phase Leggett frequency and β_L is the polar angle of the Cooper pair orbital angular momentum, measured from the direction of the static magnetic field. In the absence of gravity waves, the minimum energy configuration corresponds to the so-called flare-out texture⁶⁵. For low magnon numbers, such as at the end of the time crystals' decay in our experiments, the flare-out

texture with $\beta_L \propto r$ near the axis results in an approximately harmonic trapping potential with a characteristic size set by the magnetic healing length ξ_H^{26} . However, for large magnon numbers, the potential is heavily modified and can even become self-bound or box-like or box-like total trapping potential is a combination of the magnetic and textural parts.

For zero or low pinch coil currents the magnetic part of the potential becomes less important than the textural part. The surface energy orients the orbital angular vector perpendicular to the surface, setting $\beta_L = \pi/2$ at container walls and $\beta_L = 0$ at the free surface. The spatial variation of β_L creates the surface trap, which can additionally be identified by the faster magnon relaxation rate¹⁸.

Optomechanical Hamiltonian

We describe the combination of a time crystal in the superlfuid trap and the moving free surface as an optomechanical system with the Hamiltonian

$$\begin{split} \hat{H} &= \hbar \tilde{\omega}_{\text{TC}} \hat{a}^{\dagger} \hat{a} + \hbar \omega_{\text{m}} \hat{b}^{\dagger} \hat{b} + 2\pi \hbar g_{1} \hat{a}^{\dagger} \hat{a} \left(\hat{b}^{\dagger} + \hat{b} \right) + 2\pi \hbar g_{2} \hat{a}^{\dagger} \hat{a} \left(\hat{b}^{\dagger} + \hat{b} \right)^{2} \\ &+ \text{mech.drive} + \text{damping,} \end{split} \tag{M18}$$

where \hat{a}^{\dagger} and \hat{a} are magnon creation and annihilation operators, \hat{b}^{\dagger} and \hat{b} are mechanical mode quanta (here ripplons) creation and annihilation operators, g_1 and g_2 are the linear and quadratic coupling constants, respectively, and $\omega_{\rm m}$ corresponds to the resonance frequency of the mechanical mode. The first "cavity" term on the right-hand-side originates from equivalence of the time crystal frequency and magnon chemical potential for magnon CTC. We follow approach of Ref. 67 but the laser-drive-like terms are not relevant to our experiments and do not appear in Eq. (M18).

Eq. (1) in the main text can be derived from Eq. (M18) by the following substitutions: $g_2 \rightarrow g$, $g_1 \rightarrow 2g\theta_0$, and $\tilde{\omega}_{TC} \rightarrow \omega_0 + 2\pi g\theta_0^2$, where θ_0 is an effective static tilt of the surface in the absence of oscillations. Thus, tilting the free surface with respect to the gravity potential results in the modulation of the time crystal frequency. Note that by changing geometry (expressed as θ_0), the coupling can be smoothly tuned from quadratic to predominantly linear.

For mechanical motion as given in Eq. (M15), we get

$$\begin{split} \Delta\omega_{\text{TC}} &= 2\pi g \left[-\frac{1}{2}\theta_{\text{max}}^2 \cos(2\omega t) \right. \\ &\left. -2\theta_{\text{max}}\theta_0 \sin(\omega t) + \theta_0^2 + \frac{1}{2}\theta_{\text{max}}^2 \right], \end{split} \tag{M19}$$

where $\Delta\omega_{TC} = \omega_{TC}(t) - \omega_0$. From Eq. (M19), one can see that there are components at both ω and 2ω . The average frequency reads

$$\langle \Delta \omega_{\text{TC}} \rangle_t = 2\pi g \left(\theta_0^2 + \frac{1}{2} \theta_{\text{max}}^2 \right),$$
 (M20)

that is, the mean frequency increases as $\propto \frac{1}{2}g\theta_{\text{max}}^2$. The origin of g from free-energy considerations in the superfluid is discussed in the supplemental material.

Data availability

The data used in this study are available in the Zenodo database under accession code DOI:10.5281/zenodo.16947851.

References

- Wilczek, F. Quantum time crystals. Phys. Rev. Lett. 109, 160401 (2012).
- Sacha, K. & Zakrzewski, J. Time crystals: a review. Rep. Prog. Phys. 81, 016401 (2017).

- Bruno, P. Impossibility of spontaneously rotating time crystals: a nogo theorem. *Phys. Rev. Lett.* 111, 070402 (2013).
- Watanabe, H. & Oshikawa, M. Absence of quantum time crystals. *Phys. Rev. Lett.* 114, 251603 (2015).
- Kongkhambut, P. et al. Observation of a continuous time crystal. Science 377, 670-673 (2022).
- Liu, T., Ou, J.-Y., MacDonald, K. F. & Zheludev, N. I. Photonic metamaterial analogue of a continuous time crystal. *Nat. Phys.* 19, 986–991 (2023).
- Greilich, A. et al. Robust continuous time crystal in an electronnuclear spin system. *Nat. Phys.* 20, 631–636 (2024).
- Wu, X. et al. Dissipative time crystal in a strongly interacting Rydberg gas. Nat. Phys. 20, 1389–1394 (2024).
- Carraro-Haddad, I. et al. Solid-state continuous time crystal in a polariton condensate with a built-in mechanical clock. Science 384, 995–1000 (2024).
- Autti, S., Eltsov, V. B. & Volovik, G. E. Observation of a time quasicrystal and its transition to a superfluid time crystal. *Phys. Rev. Lett.* 120, 215301 (2018).
- Mäkinen, J. T., Autti, S. & Eltsov, V. B. Magnon Bose-Einstein condensates: From time crystals and quantum chromodynamics to vortex sensing and cosmology. *Appl. Phys. Lett.* **124**, 100502 (2024).
- Zhang, J. et al. Observation of a discrete time crystal. Nature 543, 217–220 (2017).
- Mi, X. et al. Time-crystalline eigenstate order on a quantum processor. Nature 601, 531–536 (2021).
- Wang, X. et al. Metasurface-based realization of photonic time crystals. Sci. Adv. 9, eadg7541 (2023).
- 15. Giergiel, K. et al. Creating big time crystals with ultracold atoms. *N. J. Phys.* **22**, 085004 (2020).
- Smits, J., Liao, L., Stoof, H. T. C. & van der Straten, P. Observation of a space-time crystal in a superfluid quantum gas. *Phys. Rev. Lett.* 121, 185301 (2018).
- Kreil, A. J. E. et al. Tunable space-time crystal in room-temperature magnetodielectrics. *Phys. Rev. B* 100, 020406 (2019).
- Autti, S. et al. AC Josephson effect between two superfluid time crystals. Nat. Mater. 20, 171–174 (2021).
- Autti, S. et al. Nonlinear two-level dynamics of quantum time crystals. Nat. Commun. 13, 3090 (2022).
- Giergiel, K., Hannaford, P. & Sacha, K. Time-tronics: from temporal printed circuit board to quantum computer. arXiv preprint arXiv:2406.06387 (2024).
- Aspelmeyer, M., Kippenberg, T. J. & Marquardt, F. Cavity optomechanics. Rev. Mod. Phys. 86, 1391–1452 (2014).
- Shkarin, A. B. et al. Quantum optomechanics in a liquid. *Phys. Rev. Lett.* 122, 153601 (2019).
- 23. Volovik, G. E. Twenty years of magnon Bose condensation and spin current superfluidity in ³He-B. *J. Low. Temp. Phys.* **153**, 266 (2008).
- Bunkov, Yu. M. & Volovik, G. E. Spin superfluidity and magnon Bose-Einstein condensation. In Bennemann, K. H. & Ketterson, J. B. (eds.) Novel Superfluids, vol. 1 of International Series of Monographs on Physics 156, chap. 4, 253–311 (Oxford University Press, London, 2013).
- Thompson, J. D. et al. Strong dispersive coupling of a highfinesse cavity to a micromechanical membrane. *Nature* 452, 72–75 (2008).
- Autti, S. et al. Self-trapping of magnon Bose-Einstein condensates in the ground state and on excited levels: From harmonic to box confinement. *Phys. Rev. Lett.* **108**, 145303 (2012).
- Heikkinen, P. J. et al. Relaxation of Bose-Einstein condensates of magnons in magneto-textural traps in superfluid ³He-B. J. Low. Temp. Phys. 175, 3 (2014).

- Manninen, M. S., Rysti, J., Todoshchenko, I. & Tuoriniemi, J. Quasiparticle damping of surface waves in superfluid ³He and ⁴He. *Phys. Rev. B* 90, 224502 (2014).
- Blaauwgeers, R. et al. Quartz tuning fork: thermometer, pressureand viscometer for helium liquids. J. Low. Temp. Phys. 146, 537 (2007).
- Heikkinen, P. J., Autti, S., Eltsov, V. B., Haley, R. P. & Zavjalov, V. V. Microkelvin thermometry with Bose-Einstein condensates of magnons and applications to studies of the AB interface in superfluid ³He. J. Low. Temp. Phys. 175, 681 (2014).
- Martin, H. Experiments on the thermal transport properties of superfluid ³He at ultra-low temperatures. Ph.D. thesis, Doctoral dissertation, Lancaster University, UK (2006).
- De Graaf, R., Eltsov, V., Heikkinen, P., Hosio, J. & Krusius, M. Textures of superfluid ³He-B in applied flow and comparison with hydrostatic theory. J. Low. Temp. Phys. 163, 238–261 (2011).
- 33. Thuneberg, E. V. Hydrostatic theory of superfluid ³He-B. *J. Low. Temp. Phys.* **122**, 657 (2001).
- Autti, S. et al. Transport of bound quasiparticle states in a twodimensional boundary superfluid. Nat. Commun. 14, 6819 (2023).
- 35. Barzanjeh, S. et al. Optomechanics for quantum technologies. *Nat. Phys.* **18**, 15–24 (2022).
- Abramovici, A. et al. Ligo: the laser interferometer gravitationalwave observatory. Science 256, 325–333 (1992).
- Accadia, T. et al. Virgo: a laser interferometer to detect gravitational waves. J. Instrum. 7, P03012 (2012).
- Akutsu, T. et al. Overview of KAGRA: detector design and construction history. Prog. Theor. Exp. Phys. 2021, 05A101 (2020).
- Piotrowski, J. et al. Simultaneous ground-state cooling of two mechanical modes of a levitated nanoparticle. *Nat. Phys.* 19, 1009–1013 (2023)
- de Lépinay, L. M., Ockeloen-Korppi, C. F., Woolley, M. J. & Sillanpää, M. A. Quantum mechanics-free subsystem with mechanical oscillators. Science 372, 625–629 (2021).
- 41. Chen, D., Peng, Z., Li, J., Chesi, S. & Wang, Y. Discrete time crystal in an open optomechanical system. *Phys. Rev. Res.* **6**, 013130 (2024).
- 42. Machado, J. D. P., Slooter, R. J. & Blanter, Y. M. Quantum signatures in quadratic optomechanics. *Phys. Rev. A* **99**, 053801 (2019).
- 43. Fortier, T. & Baumann, E. 20 years of developments in optical frequency comb technology and applications. *Commun. Phys.* **2**, 153 (2019).
- 44. Lesko, D. M. B. et al. A six-octave optical frequency comb from a scalable few-cycle erbium fibre laser. *Nat. Photonics* **15**, 281–286 (2021).
- 45. Saglamyurek, E. et al. Storing short single-photon-level optical pulses in Bose-Einstein condensates for high-performance quantum memory. *N. J. Phys.* **23**, 043028 (2021).
- Gao, C. et al. Axion wind detection with the homogeneous precession domain of superfluid helium-3. *Phys. Rev. Lett.* 129, 211801 (2022).
- 47. Baker, C. G. et al. Optomechanical dark matter instrument for direct detection. *Phys. Rev. D.* **110**, 043005 (2024).
- Mäkinen, J. T. et al. Half-quantum vortices and walls bounded by strings in the polar-distorted phases of topological superfluid ³He. Nat. Commun. 10, 237 (2019).
- Ivanov, D. A. Non-abelian statistics of half-quantum vortices in pwave superconductors. Phys. Rev. Lett. 86, 268–271 (2001).
- Kamppinen, T., Mäkinen, J. T. & Eltsov, V. B. Superfluid ⁴He as a rigorous test bench for different damping models in nanoelectromechanical resonators. *Phys. Rev. B* **107**, 014502 (2023).
- Hao Jiang, T. & Jing, J. Realising mechanical dynamical casimir effect with low-frequency oscillator. *Phys. Rev. A* 111, 022811 (2025).

- 52. Lambrecht, A., Jaekel, M.-T. & Reynaud, S. Motion induced radiation from a vibrating cavity. *Phys. Rev. Lett.* 77, 615–618 (1996).
- 53. Yamamoto, K. et al. Non-reciprocal pumping of surface acoustic waves by spin wave resonance. *J. Phys. Soc. Jpn.* **89**, 113702 (2020).
- Kansanen, K. S. U., Tassi, C., Mishra, H., Sillanpää, M. A. & Heikkilä, T. T. Magnomechanics in suspended magnetic beams. *Phys. Rev. B* 104, 214416 (2021).
- 55. Borisenko, I. V. et al. Direct evidence of spatial stability of Bose-Einstein condensate of magnons. *Nat. Commun.* **11**, 1691 (2020).
- 56. Blažková, M. et al. Vibrating quartz fork: a tool for cryogenic helium research. *J. Low. Temp. Phys.* **150**, 525–535 (2008).
- 57. Heikkinen, P. J. Magnon Bose-Einstein condensate as a probe of topological superfluid. Ph.D. thesis, Aalto University School of Science https://aaltodoc.aalto.fi/handle/123456789/20580. (2016).
- 58. Wheatley, J. C. Experimental properties of superfluid ³He. *Rev. Mod. Phys.* 47, 415 (1975).
- 59. Autti, S. et al. Fundamental dissipation due to bound fermions in the zero-temperature limit. *Nat. Commun.* **11**, 4742 (2020).
- 60. Case, K. M. & Parkinson, W. C. Damping of surface waves in an incompressible liquid. *J. Fluid Mech.* **2**, 172 (1957).
- 61. Matsumoto, K., Okuda, Y., Suzuki, M. & Misawa, S. Surface tension maximum of liquid ³He Experimental study. *J. Low. Temp. Phys.* **125**, 59 (2001).
- 62. Michel, G. Three-wave interactions among surface gravity waves in a cylindrical container. *Phys. Rev. Fluids* **4**, 012801 (2019).
- 63. Nicolás, J. A. Effects of static contact angles on inviscid gravity-capillary waves. *Phys. Fluids* **17**, 022101 (2005).
- 64. Miles, J. W. Internally resonant surface waves in a circular cylinder. *J. Fluid Mech.* **149**, 1–14 (1984).
- 65. Smith, H., Brinkman, W. F. & Engelsberg, S. Textures and NMR in superfluid ³He-(B). *Phys. Rev. B* **15**, 199–213 (1977).
- Autti, S., Heikkinen, P. J., Volovik, G. E., Zavjalov, V. V. & Eltsov, V. B. Propagation of self-localized Q-ball solitons in the ³He universe. *Phys. Rev. B* 97, 014518 (2018).
- Amitai, E., Lörch, N., Nunnenkamp, A., Walter, S. & Bruder, C. Synchronization of an optomechanical system to an external drive. *Phys. Rev. A* 95, 053858 (2017).
- 68. Forstner, S. et al. Dynamic interaction between chiral currents and surface waves in topological superfluids: a pathway to detect Majorana fermions? https://arxiv.org/abs/2403.19469. (2024).

Acknowledgements

We thank G. E. Volovik, M. Krusius, M. A. Silaev, I. A. Todoshchenko, M. S. Manninen, J. T. Tuoriniemi, and L. Mercier de Lépinay for stimulating discussions. The research was done using facilities of the OtaNano infrastructure supported by the Aalto University. We acknowledge the computational resources provided by the Aalto Science-IT project. The work is supported by the Research Council of Finland with Project No. 370532 (V. B. Eltsov). J. T. Mäkinen acknowledged financial support from Research Council of Finland with Project No. 370493, P. J. Heikkinen acknowledges financial support from the Väisälä foundation of the Finnish Academy of Science and Letters and from the Finnish Cultural Foundation, and S. Autti acknowledges financial support from the UK EPSRC (EP/W015730/1) and Jenny and Antti Wihuri Foundation.

Author contributions

The manuscript was written by J.T.M. and S.A., with contributions from P.J.H. and V.B.E. Experiments were conducted by P.J.H., S.A., V.V.Z., and V.B.E. Theoretical analysis was led by J.T.M., with contributions from P.J.H., S.A., and V.B.E. J.T.M. analysed the data and prepared the figures. The project was supervised by V.B.E. All authors discussed the results.

Competing interests

The authors declare no competing interests.

Additional information

Supplementary information The online version contains supplementary material available at https://doi.org/10.1038/s41467-025-64673-8.

Correspondence and requests for materials should be addressed to J. T. Mäkinen.

Peer review information *Nature Communications* thanks the anonymous reviewers for their contribution to the peer review of this work. A peer review file is available.

Reprints and permissions information is available at http://www.nature.com/reprints

Publisher's note Springer Nature remains neutral with regard to jurisdictional claims in published maps and institutional affiliations.

Open Access This article is licensed under a Creative Commons Attribution-NonCommercial-NoDerivatives 4.0 International License, which permits any non-commercial use, sharing, distribution and reproduction in any medium or format, as long as you give appropriate credit to the original author(s) and the source, provide a link to the Creative Commons licence, and indicate if you modified the licensed material. You do not have permission under this licence to share adapted material derived from this article or parts of it. The images or other third party material in this article are included in the article's Creative Commons licence, unless indicated otherwise in a credit line to the material. If material is not included in the article's Creative Commons licence and your intended use is not permitted by statutory regulation or exceeds the permitted use, you will need to obtain permission directly from the copyright holder. To view a copy of this licence, visit http://creativecommons.org/licenses/by-nc-nd/4.0/.

© The Author(s) 2025